

# Dark matter annihilation radiation in hydrodynamic simulations of Milky Way haloes

Matthieu Schaller<sup>1\*</sup>, Carlos S. Frenk<sup>1</sup>, Tom Theuns<sup>1</sup>, Francesca Calore<sup>2</sup>,  
Gianfranco Bertone<sup>2</sup>, Nassim Bozorgnia<sup>2</sup>, Robert A. Crain<sup>3</sup>, Azadeh Fattahi<sup>4</sup>,  
Julio F. Navarro<sup>4,5</sup>, Till Sawala<sup>1</sup> & Joop Schaye<sup>6</sup>

<sup>1</sup>*Institute for Computational Cosmology, Durham University, South Road, Durham, UK, DH1 3LE*

<sup>2</sup>*GRAPPA, University of Amsterdam, Science Park 904, 1090 GL Amsterdam, The Netherlands*

<sup>3</sup>*Astrophysics Research Institute, Liverpool John Moores University, 146 Brownlow Hill, Liverpool L3 5RF, UK*

<sup>4</sup>*Department of Physics and Astronomy, University of Victoria, 3800 Finnerty Road, Victoria, British Columbia V8P 5C2, Canada*

<sup>5</sup>*Senior CIFAR Fellow*

<sup>6</sup>*Leiden Observatory, Leiden University, Postbus 9513, 2300 RA Leiden, The Netherlands*

26 November 2015

## ABSTRACT

We obtain predictions for the properties of cold dark matter annihilation radiation using high resolution hydrodynamic zoom-in cosmological simulations of Milky Way-like galaxies (APOSTLE project) carried out as part of the “Evolution and Assembly of GaLaxies and their Environments” (EAGLE) programme. Galactic halos in the simulation have significantly different properties from those assumed in the “standard halo model” often used in dark matter detection studies. The formation of the galaxy causes a contraction of the dark matter halo, whose density profile develops a steeper slope than the Navarro-Frenk-White (NFW) profile between  $r \approx 1.5$  kpc and  $r \approx 10$  kpc. At smaller radii,  $r \lesssim 1.5$  kpc, the halos develop a flatter than NFW slope. This unexpected feature may be specific to our particular choice of subgrid physics model but nevertheless the dark matter density profiles agree within 30% as the mass resolution is increased by a factor 150. The inner regions of the halos are almost perfectly spherical (axis ratios  $b/a > 0.97$  within  $r = 1$  kpc) and there is no offset larger than 45 pc between the centre of the stellar distribution and the centre of the dark halo. The morphology of the predicted dark matter annihilation radiation signal is in broad agreement with  $\gamma$ -ray observations at large Galactic latitudes ( $b \gtrsim 3^\circ$ ). At smaller angles, the inferred signal in one of our four galaxies is similar to that which is observed but it is significantly weaker in the other three.

**Key words:** cosmology: theory, dark matter, gamma-rays: galaxies, Galaxy: centre, methods: numerical

## 1 INTRODUCTION

Uncovering the unknown nature of the dark matter is one of the greatest challenges of modern cosmology and particle physics. Since the original suggestion that the dark matter might consist of massive, cold, weakly interactive, neutral particles, a large body of empirical evidence has consolidated this hypothesis which, however, can only be confirmed by the detection of the particles themselves. Among the possible candidates, supersymmetric particles (see Jungman et al. 1996, for a review) such as neutralinos are attractive options that current particle accelerator experiments might detect.

An interesting property of many particle candidates for cold

dark matter is that they annihilate into standard model particles, including photons. This opens up the exciting possibility of attempting to detect such photons from space. The requirement that weakly interacting particles provide the measured dark matter density in the Universe today suggests a plausible particle mass range of order  $m_\chi = 10 - 1000$  GeV, leading to the emission of  $\gamma$ -ray photons in or below that energy range when two dark matter particles annihilate (see review by Bertone et al. 2005).

The Large Area Telescope aboard the Gamma-Ray Space Telescope (*Fermi*) (Gehrels & Michelson 1999) has, over the last few years, produced the most detailed maps of the  $\gamma$ -ray sky, covering a large energy range (20 MeV – 500 GeV) with a resolution of a few arcmin at the highest energy end of the spectrum. Analysing the *Fermi* data around the Galactic Centre (GC), a number of authors (Goodenough & Hooper 2009; Hooper & Goodenough 2011; Hooper & Linden 2011; Abazajian & Kaplinghat

\* E-mail: matthieu.schaller@durham.ac.uk

2012; Gordon & Macías 2013; Hooper & Slatyer 2013; Macias & Gordon 2014; Daylan et al. 2014; Abazajian et al. 2014; Calore et al. 2015b) have claimed the detection of extended diffuse excess emission above the other known astrophysical sources. This excess emission, peaking at  $E \approx 2$  GeV, was found to be broadly consistent with the expected signal from dark matter annihilation. In particular, the flux decreases with distance from the GC as  $r^{-\Gamma}$  with slope,  $\Gamma = 2.2 - 2.4$ , only slightly steeper than the asymptotic inner slope,  $\Gamma = 2$ , of flux originating from the NFW (Navarro et al. 1996b, 1997) density profiles found in dark matter only simulations of halos.

However, potential systematic effects in the analysis of the  $\gamma$ -ray data could be introduced by incorrect point source subtraction or the modelling of the diffuse backgrounds (Ackermann et al. 2012). Alongside the dark matter interpretation of the Galactic Centre excess, astrophysical explanations have been proposed. For example, a population of as yet unresolved millisecond pulsars (MSP) (Abazajian 2011; Gordon & Macías 2013; Yuan & Zhang 2014; Cholis et al. 2015b) or young pulsars (O’Leary et al. 2015) associated with the bulge<sup>1</sup> of the Milky Way. In contrast to the conclusions of Hooper et al. (2013) and Cholis et al. (2015b), Bartels et al. (2015) and Lee et al. (2015) have argued that the excess could be due to such a pulsar population. Alternatively, Linden et al. (2012); Carlson & Profumo (2014); Petrović et al. (2014) and Cholis et al. (2015a) have suggested that the excess could originate from the injection of very high energy cosmic rays during past activity in the Galactic Centre.

Besides the spectral shape, another property that can help distinguish the potential sources of  $\gamma$ -rays contributing to the excess is the morphology of the signal. A dark matter origin would require the excess to extend over tens of degrees on the sky (Springel et al. 2008b; Serpico & Zaharijas 2008; Nezri et al. 2012). An excess with the same spectral shape extending over a large angular range, with emissivity decreasing with distance from the GC, would strengthen the interpretation of the excess as originating from dark matter annihilation. Using multiple regions between  $2^\circ$  and  $20^\circ$  from the GC and a large range of Galactic diffuse emission (GDE) models, Calore et al. (2015b) found that the excess emission is consistent with a dark matter particle of mass  $m_\chi = 49_{-5.4}^{+6.4}$  GeV annihilating into a  $b\bar{b}$  quark pair then producing photons and is distributed following a generalised NFW profile (gNFW, see equation 1 below) with a slope  $\gamma = 1.26 \pm 0.15$ . A similar spatial distribution was found by Daylan et al. (2014) who suggested a slope for the inner profile in the range  $\gamma = 1.1 - 1.3$ . With the increasing precision of these measurements and of the foreground modelling, it has become crucial to refine the theoretical models for the distribution of dark matter at the centre of galaxies in a  $\Lambda$ CDM context. Characterising the dark matter profile slope and sphericity as well as investigating the potential offset between the dark matter and the GC are all important tasks for theorists.

Work based on dark matter only simulations has shown that the dark matter is distributed following an NFW density profile with a scale length,  $r_s$ , which varies with halo mass (e.g. Navarro et al. 1997; Neto et al. 2007; Duffy et al. 2008; Dutton & Macciò 2014). Higher-resolution simulations (Springel et al. 2008a) have shown that the very inner parts of dark matter profiles might be slightly shallower than the asymptotic NFW slope of  $\gamma = 1$  (Navarro et al. 2010). Similarly, predictions for the signal com-

ing from subhaloes have also been made using these simulations (Kuhlen et al. 2008; Springel et al. 2008b), effectively proposing a test of the cold dark matter paradigm. At the other end of the halo mass range, Gao et al. (2012) argued that nearby rich clusters provide a signal with a higher signal-to-background ratio than the Milky Way’s satellites. Thus far observational measurements have proved inconclusive and the only claimed detection comes from the centre of our own Milky Way, where precise predictions from dark matter simulations have been made (Springel et al. 2008b).

However, these studies all ignored the effects of the forming galaxy on the structure of the dark matter halo. Mechanisms such as dark matter contraction (e.g. Barnes & White 1984; Blumenthal et al. 1986; Gnedin et al. 2004) can drag dark matter towards the centre, steepening the profile. Conversely, perturbations to the potential, due for instance to feedback from stars or supermassive black holes or the formation of a bar, can lead to a flattening of the very central regions (e.g. Navarro et al. 1996a; Weinberg & Katz 2002; Mashchenko et al. 2006; Pontzen & Governato 2012). The correct balance between these mechanisms can only be understood by performing high-resolution hydrodynamic simulations of Milky Way-like galaxies using a physical model validated by comparison with a wide range of other observables.

In this study we use two “zoom” simulations of Local Group environments (the APOSTLE project: Sawala et al. 2015; Fattahi et al. 2015) performed within the framework of the “Evolution and Assembly of GaLaxies and their Environments” (EAGLE) suite (Schaye et al. 2015; Crain et al. 2015). These simulations have been shown to reproduce a large number of observables of the galaxy population at low and high redshifts, as well as the satellite galaxy luminosity functions of the Milky Way and Andromeda galaxies with unprecedented accuracy. Schaller et al. (2015a) showed that the EAGLE simulations produce galaxies with rotation curves that are in unprecedented agreement with observations of field galaxies, suggesting that the matter distribution in the simulated galaxies is realistic and that the main that effects of baryons on halos are accurately captured by the simulations. Note, however, that Calore et al. (2015a) showed that the goodness of fit of the simulated data to the observed Milky Way rotation curve is lower in the highest resolution zoomed-in simulations. The EAGLE simulations therefore provide an excellent test-bed for the interpretation and analysis of the Fermi excess.

This paper is structured as follows. In Section 2 we introduce the simulation setup used. We investigate the dark matter density profiles of our halos in Section 3 and analyse the dependence of the annihilation signal on the angle with respect to the Galactic Centre in Section 4. We summarise our findings and conclude in Section 5.

Throughout this paper, we assume a *WMAP7* flat  $\Lambda$ CDM cosmology (Komatsu et al. 2011) ( $h = 0.704$ ,  $\Omega_b = 0.0455$ ,  $\Omega_m = 0.272$  and  $\sigma_8 = 0.81$ ), express all quantities without  $h$  factors and assume a distance from the GC to the Sun of  $r_\odot = 8.5$  kpc.

## 2 THE SIMULATIONS

The simulations used in this study are based on the EAGLE simulation code (Schaye et al. 2015; Crain et al. 2015). We summarize here the parts of model relevant to our discussion.

<sup>1</sup> The thick disk population of MSPs and pulsars are unlikely to contribute more than 10% to the GeV excess (Calore et al. 2014).

## 2.1 Simulation code and subgrid models

The EAGLE code is based on a substantially modified version of the GADGET code, last described by Springel (2005). The modifications include the use of a state-of-the-art implementation of Smoothed Particle Hydrodynamics (SPH), called ANARCHY (Dalla Vecchia (in prep.), see also Schaller et al. 2015c), based on the pressure-entropy formulation of SPH (Hopkins 2013). Gravitational interactions are computed using a Tree-PM scheme.

The cooling of gas and its interaction with the background radiation is implemented following the recipe of Wiersma et al. (2009a) who tabulated photoheating and cooling rates element-by-element (for the 11 most important elements) in the presence of the UV and X-ray backgrounds inferred by Haardt & Madau (2001). To prevent artificial fragmentation, a pressure floor in the form of an effective equation of state,  $P_{\text{eos}} \propto \rho^{4/3}$ , designed to mimic the mixture of phases in the interstellar medium (ISM) (Schaye & Dalla Vecchia 2008), is applied to the cold and dense gas. Star formation is implemented using a pressure-dependent prescription that by construction reproduces the observed Kennicutt-Schmidt star formation law (Schaye & Dalla Vecchia 2008) and uses a density threshold that captures the metallicity dependence of the transition from the warm, atomic to the cold, molecular gas phase (Schaye 2004). Star particles are treated as single stellar populations with a Chabrier (2003) initial mass function (IMF) evolving along the tracks advocated by Portinari et al. (1998). Metals from supernovae (SNe) and AGB stars are injected into the ISM following the model of Wiersma et al. (2009b) and stellar feedback is implemented via the stochastic injection of thermal energy into the gas neighbouring newly-formed star particles as described by Dalla Vecchia & Schaye (2012). Galactic winds hence form naturally without having to impose a direction, velocity or mass loading factor. The amount of energy injected into the ISM per feedback event is dependent on the local gas metallicity and density in an attempt to take into account the unresolved structure of the ISM (Schaye et al. 2015; Crain et al. 2015). Supermassive black hole seeds are injected in halos above  $10^{10} h^{-1} M_{\odot}$  and grow through mergers and the accretion of low angular momentum gas (Rosas-Guevara et al. 2015; Schaye et al. 2015). AGN feedback is modelled by stochastically injecting thermal energy into the gas directly surrounding the black hole (Booth & Schaye 2009; Dalla Vecchia & Schaye 2012). Halos are identified using the FOF algorithm (Davis et al. 1985) and substructures within them are identified in post-processing using the SUBFIND code (Dolag et al. 2009).

The subgrid model was calibrated (by adjusting the efficiency of stellar feedback and the accretion rate onto black holes) so as to reproduce the present day stellar mass function and galaxy sizes, as well as the relation between galaxy stellar masses and supermassive black hole masses (Schaye et al. 2015; Crain et al. 2015). As argued by Schaye et al. (2015) (Sec. 2), numerical convergence in the traditional sense (*strong* convergence) cannot be achieved when new physical processes are resolved at each resolution. In this case, the free parameters of the model should be re-calibrated to match the same pre-defined set of observables (*weak* convergence). This can be done in cosmological simulations of representative periodic volumes (Crain et al. 2015), but it is much more difficult to achieve for “zoom-in” simulations of a few objects. In this case, even weak convergence is difficult to establish (See Sec. 3.3).

## 2.2 Selection of Milky Way halos

The two volumes used in this work are zoom resimulations of regions extracted from a dark matter only simulation of  $100^3 \text{ Mpc}^3$  with  $1620^3$  particles. The halos were selected to match the observed dynamical constraints of the Local Group (APOSTLE project: Sawala et al. 2015; Fattahi et al. 2015). Each volume contains a pair of halos in the mass range  $M_{200} = 5 \times 10^{11} M_{\odot}$  to  $M_{200} = 2.5 \times 10^{12} M_{\odot}$  that will host analogues of the Milky Way and M31. We use the two halos in volumes AP-1 and AP-4 of the APOSTLE suite (see Table 2 of Fattahi et al. 2015, where other relevant data are listed). The high-resolution region encloses a sphere larger than 2.5 Mpc around the centre of mass of the two halos at  $z = 0$ . The dark matter particle mass in the zoom regions was set to  $5 \times 10^4 M_{\odot}$ , whilst the primordial gas particle mass was set to  $1 \times 10^4 M_{\odot}$ . The initial conditions were generated from  $\Lambda$ CDM power spectra using 2<sup>nd</sup> order Lagrangian perturbation theory (Jenkins 2010) and linear phases were taken from the Gaussian white noise field PANPHASIA (Jenkins 2013). The gravitational softening length was set to  $\epsilon = 134 \text{ pc}$  (Plummer equivalent) at  $z < 2.8$  and was kept fixed in comoving units at higher redshifts. Simulations without baryonic components were run with the exact same setup and are labelled as DMO in what follows.

## 3 DARK MATTER DISTRIBUTION IN THE CENTRE OF THE HALOS

In this section, we analyse the dark matter distribution of the haloes of simulated Milky Way galaxies. We consider both central galaxies in each of the two simulation volumes as Milky Way-like galaxies.

### 3.1 Profiles without baryon effects

The analysis of the GC excess is often performed using an assumed analytic density profile shape for the dark matter. This profile is a generalisation of the NFW profile for which the asymptotic inner slope is a free parameter  $\gamma$ :

$$\rho_{\text{DM}}(r) = \frac{\rho_s}{(r/r_s)^\gamma (1 + r/r_s)^{3-\gamma}} \quad (1)$$

The NFW profile is recovered for  $\gamma = 1$ . This generalized form of the density profile is not supported by numerical simulations of collisionless dark matter (e.g. Navarro et al. 2010) but is a useful way to parametrise the deviation from the NFW shape in the very centres of halos as a result of baryonic effects. As the measurements of the GC excess only span a range of a few kiloparsecs, the value of the scale radius  $r_s$  cannot be constrained observationally and is typically fixed to  $r_s = 20 \text{ kpc}$ , in broad agreement with simulation results for Milky Way-like halos (e.g. Neto et al. 2007; Dutton & Macciò 2014). The normalisation of the profile,  $\rho_s$ , is degenerate with other particle physics parameters (see Section 4) and is usually fixed by requesting that the density of dark matter at the location of the Sun<sup>2</sup> is  $\rho_{\text{DM}}(r_{\odot}) = 0.4 \text{ GeV} \cdot \text{cm}^{-3}$ , in agreement with local dynamical constraints (Catena & Ullio 2010; Iocco et al. 2011).

In order to quantify the effects of baryons on the dark matter distribution, it is worth first considering the profiles extracted from

<sup>2</sup> Note that for simplicity we use units convenient for particle physics applications. Units more friendly to astronomers are recovered using the conversion  $1 M_{\odot} \cdot \text{kpc}^{-3} = 3.795 \times 10^{-8} \text{ GeV} \cdot \text{cm}^{-3}$ .

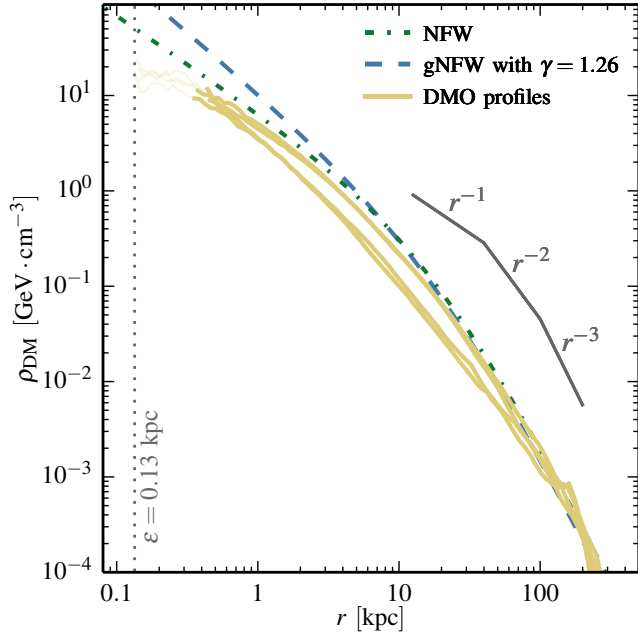


**Figure 1.** The dark matter density profiles of the four halos in the simulations without baryons (yellow solid lines). Thinner lines are used at radii smaller than the convergence radius of the simulation. The vertical dotted line indicates the simulation’s gravitational softening length. The green dot-dashed and blue dashed lines correspond to an NFW and gNFW with  $\gamma = 1.26$  profiles respectively, both normalised to  $\rho(r_\odot) = 0.4 \text{ GeV} \cdot \text{cm}^{-3}$  and with a scale-length  $r_s = 20 \text{ kpc}$ . As expected, the simulated profiles display a shape similar to the plotted NFW model, but with a lower normalisation than the standard halos.

the simulations without baryonic physics. In Fig. 1, we show the dark matter density profiles of our four halos. Thick lines are used at radii greater than the resolution limit ( $R_{\text{P}03} \approx 350 - 450 \text{ pc}$  depending on the halo) set by the criterion of Power et al. (2003) and thin lines are used at smaller radii. The softening length is indicated by the vertical dotted line. The green dot-dashed and blue dashed lines correspond to NFW and gNFW with  $\gamma = 1.26$  (the best-fitting value of Calore et al. (2015b) to the excess) profiles respectively, both normalised, as discussed above, to  $\rho_{\text{DM}}(r_\odot) = 0.4 \text{ GeV} \cdot \text{cm}^{-3}$  and with a scalelength  $r_s = 20 \text{ kpc}$ . As expected, the profiles are in good agreement with the NFW model albeit with a lower normalisation. The best-fitting NFW profile parameters to our halos are given in Table 1. The usual choice of  $r_s = 20 \text{ kpc}$  is in good agreement with our simulated halos but the normalisation of our halos is lower than what is often assumed in the literature. When baryon effects are neglected, an inner slope close to  $\gamma = 1.26$  is clearly incompatible with the simulations.

### 3.2 Profiles in the simulations with baryons

We now turn towards the dark matter profiles in the simulations including baryons. In Fig. 2, we show the dark matter density profiles of the four halos simulated with the full baryonic model. As for the previous figure, the lines are thin at radii less than the convergence radius of the simulation  $R_{\text{P}03}$  and the dashed lines correspond to the NFW and gNFW profiles normalised to  $\rho(r_\odot) = 0.4 \text{ GeV} \cdot \text{cm}^{-3}$ . The simulated profiles present two interesting features when compared to the DMO results. In the range

**Table 1.** Properties of the four simulated DMO halos (Fig. 1) and the best-fitting NFW parameters to their dark matter density profiles. The spherical overdensity masses and radii are given with respect to the critical density of the universe.

Halo	$M_{200}$ [ $M_\odot$ ]	$R_{200}$ [kpc]	$R_{\text{P}03}$ [pc]	$r_s$ [kpc]	$\rho_{\text{DM}}(r_\odot)$ [ $\text{GeV} \cdot \text{cm}^{-3}$ ]
1	$1.65 \times 10^{12}$	243.2	435	22.4	0.290
2	$1.09 \times 10^{12}$	212.0	445	20.1	0.132
3	$1.35 \times 10^{12}$	226.9	344	23.2	0.162
4	$1.39 \times 10^{12}$	229.4	358	19.8	0.281

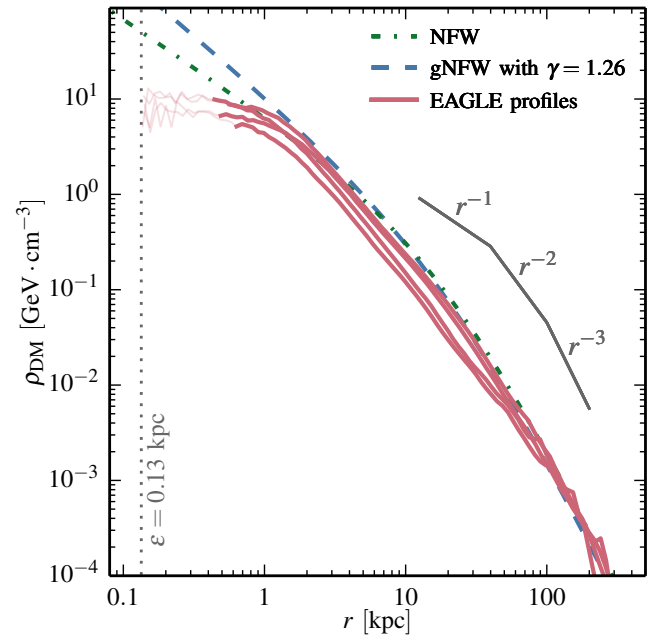


**Figure 2.** The dark matter density profiles of the four halos in the simulations with baryons physics (red solid lines). Thinner lines are used at radii smaller than the convergence radius of the simulation. The vertical dotted line indicates the simulation’s gravitational softening length. The green dot-dashed and blue dashed lines correspond to an NFW and gNFW with  $\gamma = 1.26$  profiles respectively, both normalised to  $\rho(r_\odot) = 0.4 \text{ GeV} \cdot \text{cm}^{-3}$  and with a scalelength  $r_s = 20 \text{ kpc}$ . The profiles display a logarithmic slope steeper than  $-1$  between  $r \approx 1.5 \text{ kpc}$  and  $r \approx 10 \text{ kpc}$ , in broad agreement with the profiles inferred from observations by Calore et al. (2015b). At radii  $r \leq 1 \text{ kpc}$  the profile is significantly shallower than NFW profiles are.

1.5–10 kpc, the profile is significantly steeper than an NFW profile and at radii  $r \lesssim 1 \text{ kpc}$ , the profiles display a significant flattening. Our profiles thus display a combination of dark matter contraction and a flattening further in. The properties of the dark matter distribution in the central regions are, however, particularly sensitive to the choice of subgrid model so these results, particularly the flattening of the profile, should be regarded as tentative and, by no means, as a generic prediction of  $\Lambda\text{CDM}$ .

These halos are clearly not well described over their entire radial range by any of the profiles commonly found in the literature. The main properties of the halos are given in Table 2. Note that in agreement with the findings of Schaller et al. (2015a) for the lower-resolution periodic EAGLE volume, the halo masses  $M_{200}$  (and hence radii  $R_{200}$ ) are lower than in the simulation that did

**Table 2.** Properties of the four simulated EAGLE halos (Fig. 2) and the best-fitting gNFW asymptotic slope  $\gamma$  to their dark matter density profiles in the radial range  $r > 1.5$  kpc.

Halo	$M_{200}$ [ $M_{\odot}$ ]	$R_{200}$ [kpc]	$R_{P03}$ [pc]	$\gamma$ [—]	$\rho_{DM}(r_{\odot})$ [ $\text{GeV} \cdot \text{cm}^{-3}$ ]
1	$1.56 \times 10^{12}$	238.8	559	1.38	0.310
2	$1.01 \times 10^{12}$	206.8	592	1.47	0.160
3	$1.12 \times 10^{12}$	213.7	438	1.73	0.204
4	$1.16 \times 10^{12}$	216.2	462	1.49	0.280

not include baryon physics. A consequence of the steepening of the profile due to contraction is the slight increase in the local dark matter density  $\rho_{DM}(r_{\odot})$  (column 6 of the tables), which, however, remains lower than the commonly adopted value of  $0.4 \text{ GeV} \cdot \text{cm}^{-3}$  in each case. Clearly, the simulated profiles will not be well described by a gNFW profile at radii  $r \lesssim 1.5$  kpc. It is, however, instructive to find the best-fitting profile at larger radii for comparison with the models used to characterise the Fermi excess. The best-fitting asymptotic slopes are given in column 5 of table 2. For all four halos, the slopes are steeper than the value ( $\gamma = 1.26 \pm 0.15$ ) found by Calore et al. (2015b) when modelling the GC excess. We note, however, that the simulated profiles are in broad agreement with the gNFW profile of Calore et al. (2015b) (blue dashed line), if the overall normalisation is, once again, ignored. The baryons significantly steepen the profiles at radii  $r \gtrsim 1.5$  kpc.

At radii  $r \lesssim 1.5$  kpc, the density profiles deviate significantly from the cusp seen in the DMO simulation. At the resolution limit,  $R_{P03} = 450 - 600$  pc, the simulated profiles exhibit a density between 2.5 and 4.2 times lower than the best-fit gNFW profile inferred from observations. This flattening is an important feature since the densest regions of the haloes dominate the  $\gamma$ -ray emission. No such flattening was seen in the reference EAGLE simulations, which, however, had over 200 times poorer mass resolution than the Local Group APOSTLE simulations used here. Here, the flattening is well resolved since it occurs at radii significantly larger than the Power et al. (2003) convergence radius. This indicates that the flattening is not a result of poor sampling but rather a consequence of our specific choice of subgrid model.

At high redshift all four examples had developed the cuspy central profile that is characteristic of dark matter haloes. However, the inner profiles flattened during events that are clearly associated with violent star formation in the inner few kiloparsecs. In one example, the cusp regenerated before being flattened again by a new episode of violent star formation activity. This phenomenon is reminiscent of the cusp-destroying mechanism proposed by Navarro et al. (1996a) in which the sudden removal of dense, self-gravitating gas from the centre by a starburst redistributes the binding energy of the central regions. Related processes have been seen in recent simulations, mostly of dwarf galaxies (e.g. Governato et al. 2010; Duffy et al. 2010; Macciò et al. 2012; Pontzen & Governato 2012; Teysier et al. 2013; Oñorbe et al. 2015). We defer a detailed discussion of the causes of this interesting phenomenon to a separate study.

### 3.3 Resolution and convergence considerations

In the previous two subsections, we used the criterion of Power et al. (2003) as the resolution limit of our simulations. This criterion, based on the two-body relaxation timescale, was derived using purely collisionless simulations and was designed to ensure that

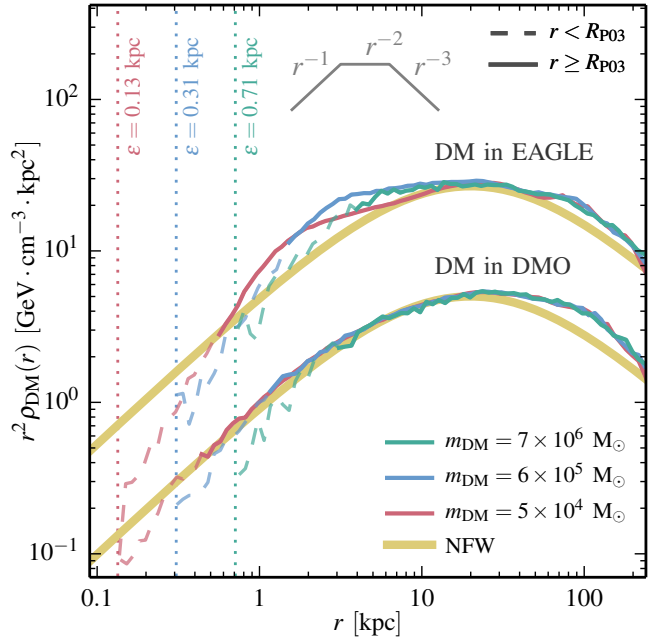


**Figure 3.** Convergence test for the dark matter profiles of one of the haloes (Halo 1) in both the simulation with baryons (upper set of lines) and without baryons (lower set of lines, rescaled by a factor of 0.2 for clarity). The green, blue and red lines correspond to the simulations with a dark matter particle mass of  $7 \times 10^6 M_{\odot}$ ,  $6 \times 10^5 M_{\odot}$  and  $5 \times 10^4 M_{\odot}$  respectively. Dashed lines are used at radii smaller than the convergence radius,  $R_{P03}$ , of each resolution. The vertical dotted lines indicate the softening length of each simulation. The thick yellow lines show an NFW profile with  $r_s = 20$  kpc. The profiles in the DMO simulation are well converged even at  $r < R_{P03}$ . In the EAGLE simulation, the profiles display a lower level of convergence but nevertheless agree within 30% at  $r > R_{P03}$ . The differences between the various resolutions are, however, smaller than the difference relative to the DMO case. The behaviour of this particular halo is typical of the four cases we simulated. These are all shown in Appendix A.

the enclosed mass at a given radius,  $R_{P03}$ , is within 10% of the value obtained using a higher resolution simulation. In the cases where baryonic effects are simulated, it is unclear whether this criterion still applies and even whether numerical convergence in the usual sense can be achieved (see discussion in Schaye et al. (2015)). Schaller et al. (2015a) demonstrated that stacked haloes, extracted from the EAGLE volumes, are well converged when using this simple criterion but it is unclear whether this remains true when individual haloes are considered. Of particular concern is the use of the pressure floor for the densest gas, which sets an artificial scale below which gas cannot be compressed. For our simulations, at all resolutions, this pressure floor ensures that Jeans lengths above  $\lambda_J \approx 750$  pc can be resolved and prevents the collapse of gas clouds of smaller sizes. It is therefore possible that the profiles may be modified by this pressure floor at radii  $r \sim \lambda_J$ , which, incidentally, is similar to the value of  $R_{P03}$  in our highest resolution simulation.

In Fig. 3 we show the density profiles (multiplied by  $r^2$  to reduce the dynamic range) of the dark matter extracted from one of our simulations run at three different resolutions, separated by factors of 12 in particle mass. The bottom set of curves are extracted from the simulation without baryons (and have been multiplied by a factor 0.2 for clarity), whilst the upper set of lines are taken from the simulations with baryons. Dashed lines are used at

radii  $r < R_{P03}$  and the vertical dotted lines indicate the softening lengths in each of the three simulations. As a guide, NFW profiles with  $r_s = 20$  kpc and the same value of  $\rho_{DM}(r_\odot)$  as the highest resolution simulation are shown using yellow lines. Similar figures for the three other haloes are shown in Appendix A.

In the DMO simulations (lower set of curves), the profiles of different resolution converge very well and, as expected, the criterion of Power et al. (2003) (which refers to the enclosed mass) provides a good, conservative, estimate of the radius above which the *density* profiles are converged. In fact, the density profiles are converged to  $r > 0.7R_{P03}$ . The profiles are very well described by the NFW functional form and show an asymptotic inner slope of  $-1$ . The deviation from NFW seen at  $r \geq 30$  kpc is due to the presence of substructures in the haloes.

The situation is different for the haloes with baryonic physics (upper set of curves). At  $r \lesssim 10$  kpc, the profiles show significant differences when the resolution is varied. Important differences are especially visible between the two highest resolutions (blue and red curves). Clearly, the criterion of Power et al. (2003) is no longer suitable because the profiles show differences even at  $r > R_{P03}$  but note that in that range all three resolutions nevertheless agree within 30%. Despite this poorer level of convergence, the profiles display similar general trends across resolution levels. The profiles are significantly steeper than NFW at  $1.5 \text{ kpc} \lesssim r \lesssim 10 \text{ kpc}$  and significantly shallower than NFW at smaller radii. These differences relative to the NFW profile are larger than the differences between the various resolution simulations, suggesting that the trends seen are a generic outcome of the subgrid model assumed in our simulation even if their exact magnitude is difficult to establish. In the remainder of this paper, we will restrict our analysis to the highest resolution simulations, but these limitations should be borne in mind when interpreting our results and evaluating the generality of our conclusions.

### 3.4 Sphericity of the distribution

In order to characterise the morphology of the dark matter annihilation signal at the centre of the Milky Way, it is interesting to study the shape of the dark matter distribution. The profiles described so far assumed a spherically symmetric dark matter density profile. With the higher precision of the measurements of the excess and the increasing understanding of the GDE, it will soon be possible to measure deviations from a perfect sphere. For instance, the presence of a “dark disc” (Read et al. 2008) would enhance the signal in the plane of the galactic disk and hence break the symmetry of the signal. This would also make the signal more difficult to disentangle from astrophysical components associated with the disk, such as point sources.

In order to test this, we computed the inertia tensor of our four halos using all the dark matter within a spherical aperture of 1 kpc from the centre. This distance corresponds to  $\approx 7^\circ$  on the sky and hence encompasses the majority of the  $\gamma$ -ray flux in the direction towards the Galactic Centre that would result from dark matter annihilation in the MW. We then compute the three eigenvalues  $a > b > c$  of the inertia tensor and report the values in Table 3 for both simulations with and without baryons.

As can be seen, the axis ratios are very close to unity, indicating only very small deviations from sphericity and hence no obvious anisotropy feature in the signal. We also find no alignment between the main axis of the dark matter distribution in the inner 1 kpc and the plane of rotation of the stars. It is interesting to note that the simulation with baryons yields more spherical distributions

**Table 3.** Axis ratios ( $a > b > c$ ) inferred from the inertia tensor of the matter within 1 kpc from the centre of the galaxies for both the halos in the DMO and EAGLE local group simulations.

Halo	DMO		EAGLE	
	$b/a$	$c/b$	$b/a$	$c/b$
1	0.888	0.973	0.989	0.953
2	0.863	0.957	0.975	0.971
3	0.850	0.984	0.981	0.941
4	0.879	0.964	0.987	0.988

close to the centre than its counterpart without baryons. We verified that repeating the exercise with apertures of 0.5, 2 and 3 kpc yields similar results.

### 3.5 Position of the centre

Another potential source of systematics in the analysis of the GC excess is the position of the centre of the dark matter distribution. If the highest-density part of the dark matter profile is offset from the centre of the stellar distribution, then this offset should be detectable in observations. In their simulation of a single Milky Way-like halo, Kuhlen et al. (2013) found a sizeable offset of 300 – 400 pc between the centre of the stellar distribution and the peak of their dark matter distribution. If such an offset was indeed present in the Milky Way, then an offset of  $\approx 2^\circ$  between the GC and the peak of the dark matter annihilation signal should be visible. In their study based on the EAGLE simulations, Schaller et al. (2015b) found that the offset between the peak of the dark matter density distribution and the centre of the stellar distribution is typically smaller than the softening length of the simulation ( $\epsilon = 700$  pc in their case). Repeating their analysis on our four simulated Milky Way halos, we find offsets between 22 and 43 pc, well below the size of the softening length ( $\epsilon = 134$  pc), indicating that the offsets are consistent with zero. For all practical purposes and given the current resolution of instruments, the centre of the dark matter distribution is hence coincident with the centre of the stellar distribution.

## 4 DARK MATTER ANNIHILATION SIGNAL

Now that the dark matter profiles have been characterised, we turn to the derivation of the corresponding annihilation signal as observed by a virtual instrument located at the position of the Sun and pointing towards the centre of the Milky Way.

### 4.1 J-factor for the simulated halos

In the case of a dark matter particle that annihilates into photons or into particles that generate photons in their decays, the photon flux (in units of  $\text{GeV}^{-1} \cdot \text{cm}^{-2} \cdot \text{s}^{-1} \cdot \text{sr}^{-1}$ ) at a given angle,  $\Psi$ , on the sky away from the GC is given by

$$\frac{dN}{dE}(\Psi) = \frac{\langle\sigma v\rangle}{8\pi m_\chi^2} \frac{dN_\gamma}{dE} I(\Psi), \quad (2)$$

where  $m_\chi$  is the mass of the dark matter particle,  $\langle\sigma v\rangle$  is its velocity averaged total annihilation cross section,  $dN_\gamma/dE$  is the averaged energy spectrum of photons produced per annihilation and

$I(\Psi)$  is the integral along the line of sight of the square of the dark matter density. This so-called ‘‘J-factor’’ reads

$$I(\Psi) = \int_{l.o.s.} \rho_{DM}^2(r(s, \Psi)) ds, \quad (3)$$

with the variable  $s$  running along the line of sight axis from  $s = 0$  to  $s = \infty$  and

$$r(s, \Psi) = \sqrt{(r_{\odot} - s \cos \Psi)^2 + (s \sin \Psi)^2} \quad (4)$$

giving the distance from the GC for a particular angle on the sky  $\Psi$  and distance to the GC,  $r_{\odot}$ . The differential intensity  $dN/dE$  is hence the product of the J-factor, given by the distribution of dark matter, and the particle physics model assumed. As a consequence, within a reasonable range, the precise normalisation of the J-factor is irrelevant since a similar signal can be recovered by altering the particle physics model. To simplify the comparison with the analysis of the GC excess, we have, thus, normalised our simulated profiles such that  $\rho_{DM}(r_{\odot}) = 0.4 \text{ GeV} \cdot \text{cm}^{-3}$ .

In the top panel of Fig. 4 we show the J-factor (Eq. 3) as a function of galactic latitude  $b$  (at galactic longitude  $l = 0^{\circ}$ ) for our four simulated profiles, normalised to the same local dark matter density. The red and yellow lines correspond to the the dark matter profiles in the simulations with and without baryons respectively. The green dot-dashed and blue dashed lines correspond to NFW and gNFW with  $\gamma = 1.26$  profiles respectively with a scale length  $r_s = 20 \text{ kpc}$  and the same normalisation local dark matter density as our normalised halos. The shape of the J-factor profile is different in the runs with and without baryons. The contraction of the dark matter due to baryons increases the J-factor by a factor of  $\approx 2$  at angles  $b \gtrsim 4^{\circ}$  from the GC, when compared to an NFW halo. In that angular range, the J-factor is also larger than the one obtained for a gNFW with a slope  $\gamma = 1.26$  (Calore et al. 2015b). Closer to the GC, the simulated J-factors display a shallower slope and values lower than the gNFW model.

## 4.2 Extrapolation of the profiles towards the centre

As most of the dark matter annihilation signal originates from the inner few hectoparsecs, it is necessary to extrapolate our findings from section 3.2 to smaller radii. As the annihilation signal increases with the square of the local density, one can ask what the highest density is that can be reached in the inner regions given the constraints on the density and enclosed mass at the smallest converged radius. Assuming that the profile is not hollow and that the logarithmic slope is monotonic, it is straightforward to show that the only asymptotic power law that can be used to extrapolate the profiles from a given radius  $r$  towards the centre has a slope  $\gamma_{\max} = 3(1 - 4\pi r^3 \rho(r)/3M(r))$  (Navarro et al. 2010). Setting  $r$  to the convergence radius of the halos,  $R_{P03}$ , we obtain slopes in the range  $\gamma_{\max} = 0.55 - 1.22$  for our four halos. The J-factors resulting from these extrapolations are shown on Fig. 4 using thin lines. They allow us to set upper bounds on the J-factor for angles  $b \lesssim 3^{\circ}$ . Even with this power-law extrapolation, the flux is lower than the gNFW profile with a slope  $\gamma = 1.26$ .

## 4.3 Gamma-ray flux morphology

In the bottom panel of Fig. 4, we show the emission at  $E = 2 \text{ GeV}$  for our J-factors, assuming the best-fitting particle physics model

of Calore et al. (2015b)<sup>3</sup>. For comparison, we show the flux inferred from the GC excess by Hooper & Goodenough (2011), Boyarsky et al. (2011), Gordon & Macías (2013), Hooper & Slatyer (2013), Daylan et al. (2014) and Abazajian et al. (2014) with the error bars indicating the  $\pm 1\sigma$  statistical error (not shown when smaller than the symbols). The observed intensities were rescaled following the procedure highlighted in Calore et al. (2015c), taking into account the assumed excess profiles. Note that individual measurements are more than  $3\sigma$  discrepant with each other. The green shaded regions indicate the best-fitting model of Calore et al. (2015b). Their model assumed a gNFW profile for the dark matter profile and used 60 GDE templates in their likelihood analysis of 10 regions of interest on the sky located around the galactic centre. The width of the green regions on the figure indicates both the statistical uncertainty and the posterior range of the GDE modelling around the best-fitting gNFW profile. The uncertainty on the slope of the profile is not shown. A similar analysis, performed by Calore et al. (2015c), of the preliminary results of the Fermi collaboration is shown as a yellow shaded region. The grey shaded region on the left of the plot indicates the radial range over which the emission from the ISM gas dominates the GDE models (Calore et al. 2015c). Similarly, the grey shaded region at the bottom of the panel indicates the level of  $\gamma$ -ray flux expected from the extended ‘‘Fermi Bubbles’’ (Su et al. 2010), thought to be the remnant of past AGN activity. We use the extrapolation, assuming a constant density, to lower latitudes of the flux estimated by Ackermann et al. (2014). The flux originating from the annihilation of dark matter is higher than the contribution of the Fermi Bubbles at angles  $b < 15^{\circ}$ , making the radial range  $2^{\circ} < b < 15^{\circ}$  ideal for the study of the excess (Calore et al. 2015c). The resolution of our simulations is, hence, well matched to this requirement.

Our simulated profiles (red lines) are in good agreement with the  $\gamma$ -ray data for angles  $b > 3^{\circ}$ . This is expected since over the relevant radial range, the profiles have a similar form to the gNFW profile with asymptotic inner slope,  $\gamma = 1.2 - 1.3$ , inferred directly from the data (assuming that the emission is due to dark matter annihilation). At smaller angles, three of the four extrapolated profiles give significantly less emission than observed, whilst the fourth is in good agreement with the data. We stress, however, that this extrapolation gives the largest power-law signal at the GC. The predicted emission at  $b < 2^{\circ}$  could be boosted by adjusting the particle physics model but there is a danger that such adjustments could lead to an overprediction of the emission at larger angles.

## 5 SUMMARY & CONCLUSION

In this study we investigated the dark matter density profiles of four Milky Way galaxies simulated using a state-of-the-art hydrodynamics code and subgrid model. We specifically focused on the inner few kiloparsecs of the dark matter distribution in order to refine earlier predictions for the properties of dark matter annihilation emission. The careful treatment of baryons in our simulations allows us to understand and analyse the effects that baryons have on the dark matter distribution. These are not negligible and give rise to haloes whose properties differ significantly from those of the ‘‘standard halo model’’ often used in dark matter detection studies. Whilst our simulations are among the highest resolution examples of their kind currently available, we are only able to establish

<sup>3</sup>  $m_{\chi} = 46.6 \text{ GeV}$ ,  $\langle\sigma v\rangle = 1.60 \times 10^{-26} \text{ cm}^3 \text{ s}^{-1}$  for a  $b\bar{b}$  final annihilation state.

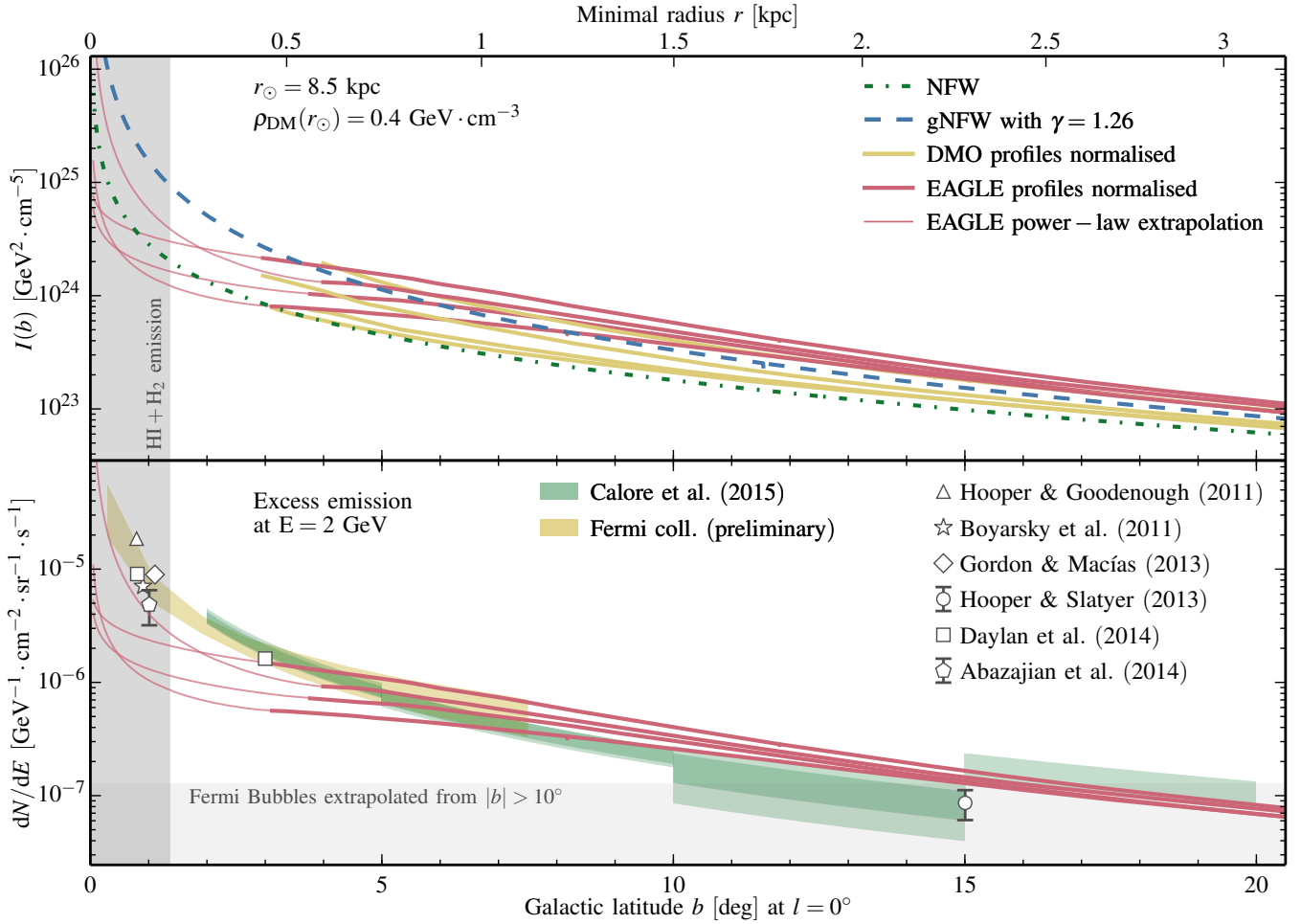


**Figure 4.** *Top panel:* The J-factor as a function of galactic latitude  $b$  inferred from our four simulated halos both with (red lines) and without (yellow lines) baryon effects. The green dot-dashed and blue dashed lines correspond to NFW and gNFW with  $\gamma = 1.26$  profiles respectively with a scale length  $r_s = 20$  kpc. To ease comparison, all profiles have been normalised to yield  $\rho_{\text{DM}}(r_\odot) = 0.4 \text{ GeV} \cdot \text{cm}^{-3}$ . The thin lines correspond to power-law extrapolations of our simulated profiles (see text). The scale at the top indicates the minimum radius intersected by a line of sight at the given galactic latitude  $b$ . *Bottom panel:* Emission at  $E = 2$  GeV for our halos assuming the best-fitting particle physics model from Calore et al. (2015c). Data points with error bars show the best-fitting models of Hooper & Goodenough (2011), Boyarsky et al. (2011), Gordon & Macías (2013), Hooper & Slatyer (2013), Daylan et al. (2014) and Abazajian et al. (2014) to the Fermi GeV excess. The green shaded regions indicate the excess emission and its statistical uncertainty for a fixed gNFW profile derived by Calore et al. (2015b) and the yellow shaded region indicates the preliminary results of the Fermi-LAT team. The vertical grey shaded region indicates the radial range where uncertainties in the GDE modelling due to  $\pi^0$  emission from HI and H<sub>2</sub> regions dominate the foreground templates used in the analysis of the data (adapted from Calore et al. 2015c). Similarly, the shaded region at the bottom indicates the flux intensity of the Fermi bubbles.

convergence within a tolerance of 30% across different resolutions over the radial range of interest (sec. 3.3). We feel that this level of convergence is sufficient to support our conclusions but higher resolution simulations will be needed to test this supposition.

We can summarise our findings as follows:

- As seen in previous simulations (e.g. Dubinski 1994; Abadi et al. 2010; Bryan et al. 2013), the central concentration of baryons significantly reduces the asphericity typical of haloes in dark matter-only simulations. The distribution of dark matter in the inner 500 pc is very close to spherical with axis ratios,  $b/a > 0.96$ , in all cases.
- There is no detectable offset between the position of the GC and the peak of the dark matter distribution. The largest offset found in our halos is 45 pc, much smaller than the softening length of the

simulations ( $\epsilon = 134$  pc).

- The condensation of baryons at the halo centre causes the halo to contract slightly. The halo density profiles end up having steeper profiles than NFW in the radial range  $r = 2 - 10$  kpc.
- In the inner 1.5 kpc, which are well resolved in our simulations the dark matter halo density profiles develop significant flattening. This feature is likely to be associated with violent star formation events that take place during the early stages of galaxy formation. It must be borne in mind that effects of this kind are sensitive to the specific subgrid physics model and, at this point, they must not be regarded as a generic prediction of the  $\Lambda$ CDM model.
- The predicted dark matter annihilation emission signal is in good agreement with the detection of extended  $\gamma$ -ray emission in excess



of the known foregrounds by the *Fermi* satellite at galactic latitudes,  $b \gtrsim 3^\circ$ , where our haloes are well resolved. A simple extrapolation of the density profiles in our simulations to smaller angles predicts a  $\gamma$ -ray flux significantly lower than is measured, in three of the four cases, suggesting possible contributions from other sources to the excess. In the fourth case, the annihilation signal from the extrapolation is in broad agreement with the reported measurements close to the Galactic Centre.

The analysis of the *Fermi* excess has so far been performed assuming a gNFW profile or other parametric profile forms for the dark matter. Future, more precise studies, would benefit from using the more realistic profile shapes derived directly from hydrodynamical simulations. This should help disentangle the signal from dark matter annihilation from the galactic diffuse emission.

## ACKNOWLEDGEMENTS

This work would have not been possible without Lydia Heck and Peter Draper's technical support and expertise. This work was supported by the Science and Technology Facilities Council (grant number ST/F001166/1); European Research Council (grant numbers GA 267291 "Cosmiway" and GA 278594 "GasAroundGalaxies") and by the Interuniversity Attraction Poles Programme initiated by the Belgian Science Policy Office (AP P7/08 CHARM). RAC is a Royal Society University Research Fellow.

This work used the DiRAC Data Centric system at Durham University, operated by the Institute for Computational Cosmology on behalf of the STFC DiRAC HPC Facility ([www.dirac.ac.uk](http://www.dirac.ac.uk)). This equipment was funded by BIS National E-infrastructure capital grant ST/K00042X/1, STFC capital grant ST/H008519/1, and STFC DiRAC Operations grant ST/K003267/1 and Durham University. DiRAC is part of the National E-Infrastructure. We acknowledge PRACE for awarding us access to the Curie machine based in France at TGCC, CEA, Bruyères-le-Châtel.

## REFERENCES

Abadi M. G., Navarro J. F., Fardal M., Babul A., Steinmetz M., 2010, *MNRAS*, **407**, 435

Abazajian K. N., 2011, *J. Cosmology Astropart. Phys.*, **3**, 10

Abazajian K. N., Kaplinghat M., 2012, *Phys. Rev. D*, **86**, 083511

Abazajian K. N., Canac N., Horiuchi S., Kaplinghat M., 2014, *Phys. Rev. D*, **90**, 023526

Ackermann M., et al., 2012, *ApJ*, **750**, 3

Ackermann M., et al., 2014, *ApJ*, **793**, 64

Barnes J., White S. D. M., 1984, *MNRAS*, **211**, 753

Bartels R., Krishnamurthy S., Weniger C., 2015, preprint, ([arXiv:1506.05104](https://arxiv.org/abs/1506.05104))

Bertone G., Hooper D., Silk J., 2005, *Phys. Rep.*, **405**, 279

Blumenthal G. R., Faber S. M., Flores R., Primack J. R., 1986, *ApJ*, **301**, 27

Booth C. M., Schaye J., 2009, *MNRAS*, **398**, 53

BoyarSKy A., Malyshev D., Ruchayskiy O., 2011, *Physics Letters B*, **705**, 165

Bryan S. E., Kay S. T., Duffy A. R., Schaye J., Dalla Vecchia C., Booth C. M., 2013, *MNRAS*, **429**, 3316

Calore F., Di Mauro M., Donato F., 2014, *ApJ*, **796**, 14

Calore F., et al., 2015a, preprint, ([arXiv:1509.02164](https://arxiv.org/abs/1509.02164))

Calore F., Cholis I., Weniger C., 2015b, *J. Cosmology Astropart. Phys.*, **3**, 38

Calore F., Cholis I., McCabe C., Weniger C., 2015c, *Phys. Rev. D*, **91**, 063003

Carlson E., Profumo S., 2014, *Phys. Rev. D*, **90**, 023015

Catena R., Ullio P., 2010, *J. Cosmology Astropart. Phys.*, **8**, 4

Chabrier G., 2003, *PASP*, **115**, 763

Cholis I., Evoli C., Calore F., Linden T., Weniger C., Hooper D., 2015a, preprint, ([arXiv:1506.05119](https://arxiv.org/abs/1506.05119))

Cholis I., Hooper D., Linden T., 2015b, *J. Cosmology Astropart. Phys.*, **6**, 43

Crain R. A., et al., 2015, *MNRAS*, **450**, 1937

Dalla Vecchia C., Schaye J., 2012, *MNRAS*, **426**, 140

Davis M., Efstathiou G., Frenk C. S., White S. D. M., 1985, *ApJ*, **292**, 371

Daylan T., Finkbeiner D. P., Hooper D., Linden T., Portillo S. K. N., Rodd N. L., Slatyer T. R., 2014, preprint, ([arXiv:1402.6703](https://arxiv.org/abs/1402.6703))

Dolag K., Borgani S., Murante G., Springel V., 2009, *MNRAS*, **399**, 497

Dubinski J., 1994, *ApJ*, **431**, 617

Duffy A. R., Schaye J., Kay S. T., Dalla Vecchia C., 2008, *MNRAS*, **390**, L64

Duffy A. R., Schaye J., Kay S. T., Dalla Vecchia C., Battye R. A., Booth C. M., 2010, *MNRAS*, **405**, 2161

Dutton A. A., Macciò A. V., 2014, *MNRAS*, **441**, 3359

Fattahi A., et al., 2015, preprint, ([arXiv:1507.03643](https://arxiv.org/abs/1507.03643))

Gao L., Frenk C. S., Jenkins A., Springel V., White S. D. M., 2012, *MNRAS*, **419**, 1721

Gehrels N., Michelson P., 1999, *Astroparticle Physics*, **11**, 277

Gnedin O. Y., Kravtsov A. V., Klypin A. A., Nagai D., 2004, *ApJ*, **616**, 16

Goodenough L., Hooper D., 2009, preprint, ([arXiv:0910.2998](https://arxiv.org/abs/0910.2998))

Gordon C., Macías O., 2013, *Phys. Rev. D*, **88**, 083521

Governato F., et al., 2010, *Nature*, **463**, 203

Haardt F., Madau P., 2001, in Neumann D. M., Tran J. T. V., eds, *Clusters of Galaxies and the High Redshift Universe Observed in X-rays*. ([arXiv:astro-ph/0106018](https://arxiv.org/abs/astro-ph/0106018))

Hooper D., Goodenough L., 2011, *Physics Letters B*, **697**, 412

Hooper D., Linden T., 2011, *Phys. Rev. D*, **84**, 123005

Hooper D., Slatyer T. R., 2013, *Physics of the Dark Universe*, **2**, 118

Hooper D., Cholis I., Linden T., Siegal-Gaskins J. M., Slatyer T. R., 2013, *Phys. Rev. D*, **88**, 083009

Hopkins P. F., 2013, *MNRAS*, **428**, 2840

Iocco F., Pato M., Bertone G., Jetzer P., 2011, *J. Cosmology Astropart. Phys.*, **11**, 29

Jenkins A., 2010, *MNRAS*, **403**, 1859

Jenkins A., 2013, *MNRAS*, **434**, 2094

Jungman G., Kamionkowski M., Griest K., 1996, *Phys. Rep.*, **267**, 195

Komatsu E., et al., 2011, *ApJS*, **192**, 18

Kuhlen M., Diemand J., Madau P., 2008, *ApJ*, **686**, 262

Kuhlen M., Guedes J., Pillepich A., Madau P., Mayer L., 2013, *ApJ*, **765**, 10

Lee S. K., Lisanti M., Safdi B. R., Slatyer T. R., Xue W., 2015, preprint, ([arXiv:1506.05124](https://arxiv.org/abs/1506.05124))

Linden T., Lovegrove E., Profumo S., 2012, *ApJ*, **753**, 41

Macciò A. V., Stinson G., Brook C. B., Wadsley J., Couchman H. M. P., Shen S., Gibson B. K., Quinn T., 2012, *ApJ*, **744**, L9

Macías O., Gordon C., 2014, *Phys. Rev. D*, **89**, 063515

Mashchenko S., Couchman H. M. P., Wadsley J., 2006, *Nature*, **442**, 539

Navarro J. F., Eke V. R., Frenk C. S., 1996a, *MNRAS*, **283**, L72

Navarro J. F., Frenk C. S., White S. D. M., 1996b, *ApJ*, **462**, 563

Navarro J. F., Frenk C. S., White S. D. M., 1997, *ApJ*, **490**, 493

Navarro J. F., et al., 2010, *MNRAS*, **402**, 21

Neto A. F., et al., 2007, *MNRAS*, **381**, 1450

Nezri E., Laval J., Teyssier R., 2012, *Phys. Rev. D*, **86**, 063524

Oñorbe J., Boylan-Kolchin M., Bullock J. S., Hopkins P. F., Kereš D., Faucher-Giguère C.-A., Quataert E., Murray N., 2015, *MNRAS*, **454**, 2092

O'Leary R. M., Kistler M. D., Kerr M., Dexter J., 2015, preprint, ([arXiv:1504.02477](https://arxiv.org/abs/1504.02477))

Petrović J., Dario Serpico P., Zaharijaš G., 2014, *J. Cosmology Astropart. Phys.*, **10**, 52

Pontzen A., Governato F., 2012, *MNRAS*, **421**, 3464

Portinari L., Chiosi C., Bressan A., 1998, *AAP*, **334**, 505

- Power C., Navarro J. F., Jenkins A., Frenk C. S., White S. D. M., Springel V., Stadel J., Quinn T., 2003, *MNRAS*, **338**, 14
- Read J. I., Lake G., Agertz O., Debattista V. P., 2008, *MNRAS*, **389**, 1041
- Rosas-Guevara Y. M., et al., 2015, *MNRAS*, **454**, 1038
- Sawala T., et al., 2015, preprint, ([arXiv:1511.01098](https://arxiv.org/abs/1511.01098))
- Schaller M., et al., 2015a, *MNRAS*, **451**, 1247
- Schaller M., Robertson A., Massey R., Bower R. G., Eke V. R., 2015b, *MNRAS*, **453**, L58
- Schaller M., Dalla Vecchia C., Schaye J., Bower R. G., Theuns T., Crain R. A., Furlong M., McCarthy I. G., 2015c, *MNRAS*, **454**, 2277
- Schaye J., 2004, *ApJ*, **609**, 667
- Schaye J., Dalla Vecchia C., 2008, *MNRAS*, **383**, 1210
- Schaye J., et al., 2015, *MNRAS*, **446**, 521
- Serpico P. D., Zaharijas G., 2008, *Astroparticle Physics*, **29**, 380
- Springel V., 2005, *MNRAS*, **364**, 1105
- Springel V., et al., 2008a, *MNRAS*, **391**, 1685
- Springel V., et al., 2008b, *Nature*, **456**, 73
- Su M., Slatyer T. R., Finkbeiner D. P., 2010, *ApJ*, **724**, 1044
- Teyssier R., Pontzen A., Dubois Y., Read J. I., 2013, *MNRAS*, **429**, 3068
- Weinberg M. D., Katz N., 2002, *ApJ*, **580**, 627
- Wiersma R. P. C., Schaye J., Smith B. D., 2009a, *MNRAS*, **393**, 99
- Wiersma R. P. C., Schaye J., Theuns T., Dalla Vecchia C., Tornatore L., 2009b, *MNRAS*, **399**, 574
- Yuan Q., Zhang B., 2014, *Journal of High Energy Astrophysics*, **3**, 1

## APPENDIX A: RESOLUTION TEST FOR ALL HALOES

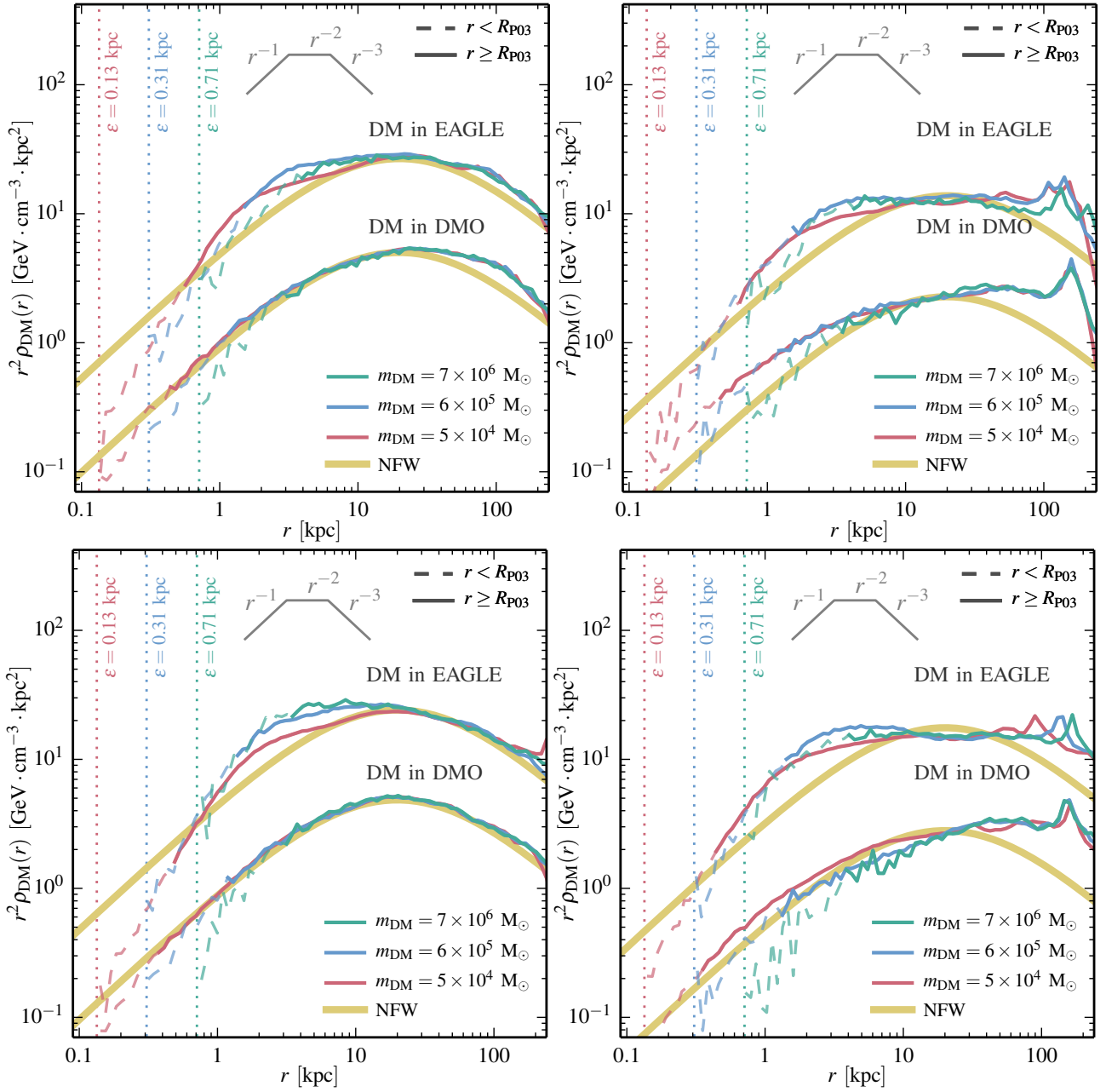


**Figure A1.** Same as Fig. 3 but for all four halos considered in this study. The DM density profiles in all four haloes agree to better than 30% at  $r < 10$  kpc.